Sunburst pattern by kinetic segregation in core-shell nanowires: a phase-field study

Roberto Bergamaschini[a,*], Francesco Montalenti[a], Leo Miglio[a]

[a] *L-NESS and Dept. of Materials Science, Università di Milano-Bicocca, via R. Cozzi 55, I-20125, Milano, Italy*

Abstract

Compositional segregation is commonly observed during the growth of III-V alloys in core-shell nanowires. Nanometer-thin stripes, enriched in one of the alloy components, are observed along the six <112> directions perpendicular to the [111]-wire axis, departing from the core to the outer shell edges in between the {110} faceted sidewalls. While it has been well established that the phenomenon occurs because of the different mobility of the alloy components, the actual mechanisms by which it happens are yet unclear. A phase-field model, coupling deposition and surface diffusion dynamics, is here developed to inspect the simultaneous evolution of the shell morphology and composition during growth. Both surface energy anisotropy and orientation-dependent growth rates are taken into account to identify their different role. Simulations reveal that the observed segregation is mainly triggered by the enhanced growth rate at the facet edges, while surface anisotropy keeps the stripes thin. Polarity effects are also included to differentiate the behavior between <112>A and <112>B orientations, so to reproduce the experimental observation of a 3-fold symmetry.

Keywords: Nanowires, Intermixing, Phase-field, Kinetic segregation, Core-shell

1. Introduction

Compositional segregation effects are very common during the epitaxy of semiconductor alloys, especially at the nanoscale. The origin can be both thermodynamic and kinetic and the resulting behavior is strongly influenced by the growth dynamics. Understanding and controlling the mechanisms driving the evolution of crystal morphology and segregation is of great importance as nonuniform composition profile seriously impact on the material properties and applications. The peculiar geometry of core-shell nanowires (NW) offers an interesting case to inspect such processes.

In particular, a "sunburst" pattern is ubiquitously observed when growing shells of III-V alloys on a NW core with [111]-axis. Nanometer-thin sheets, enriched in one of the alloy components with respect to the composition in the NW facets, are observed to develop radially along the six <112> directions, right at the corners between the six {110} sidewall facets, running across the whole shell thickness, from the core edges to the outer shell ones. In particular, the formation of Al-rich stripes has been reported in the case of lattice-matched systems such as GaAs-AlGaAs [1, 2, 3, 4, 5, 6], InGaAs-InAlAs [7, 8], GaAs-AlInP [9, 10], and also for strained systems such as GaAs-InAlAs [11]. The same behavior has been also observed for the strained system GaAs-InGaAs [11], with segregation of Ga, and for GaAsP-GaAsP core-shell NWs [12], with segregation of P. A similar sunburst segregation pattern was even recognized in the case of Ge-GeSn core-shell NWs [13, 14], despite their poor miscibility.

Notably, the reported experiments were performed by both molecular beam epitaxy and chemical vapour deposition excluding any specificity of the phenomenon with respect to the growth technique. The fact of observing similar behavior also in the case of lattice-mismatched structures, at least when strain levels are low enough, indicates a quite general mechanism. This is further sustained by the observation of analogous effects of segregation even for systems diverse from NWs, e.g. in squared GaAs/AlGaAs corner-overgrown heterostructures [15] or at facet edges in GaAs/AlGaAs epitaxial nanomembranes obtained by selective area epitaxy [16].

It is commonly recognized that the origin of the sunburst segregation process is kinetic, resulting from the different mobility of the alloy components (see [17, 18]). Indeed, the species accumulating in the stripes is in all cases the one expected to have lower mobility. A flow of material away from facet edges is then presumed to return the observed behavior. Despite this qualitative understanding, a model that could describe the segregation in a simple way with a minimum number of assumptions is not yet fully established. Some of the cited studies [2, 10, 9] hypothesize the presence of small {112} segments in between the {110} sidewalls, with self-limited size [19] of just few nanometers. In Ref. [20] it was shown that a possible interpretation of the here-discussed segregation effects could be achieved by admitting peculiar surface properties on such nanofacets, including a local reversal in the mobility ratio between the alloy components.

*Corresponding author.
Email address: roberto.bergamaschini@unimib.it (Roberto Bergamaschini)

In this study we propose a simple yet effective continuum model of the shell growth, able to capture the key factors driving the coupled evolution of morphology and composition, on the basis of a reduced set of parameters, established according to the available experimental evidences. In particular, the model is conceived in a sufficiently general way not to require the explicit introduction of the {112} nanofacets. In our continuum description of the growth front, such corners are locally rounded so to smoothly connect the {110} sides. Interestingly, some theoretical studies on the faceting of nanoparticles [21] even proposed that facet edges may be properly defined by a local rounding at the atomic scale. However, our treatment is meant to be valid in both cases as far as the rounded regions can be considered an equivalent of {112} nanofacets in our continuum limit.

The numerical implementation by a phase-field approach, detailed in the following section, allowed us to perform simulations of the shell growth in combination with intermixing. First, simple test cases are considered, in order to identify the role of both surface energy anisotropy and orientation-dependent growth rates. Then, more realistic simulations, also including polarity effects [3, 12], are developed, in good agreement with the experimental observations.

2. Phase-field model

A continuum model is exploited to reproduce by numerical simulations the coupled evolution of morphology and composition of the NW shell during its growth around the core. The $Al_xGa_{1-x}As$ alloy is here considered as reference case even if the description is valid more in general for other III-V alloys and for group-IV binary alloys. Only the two-dimensional (2D) (111) cross-section is modeled under the assumption of axial symmetry for the NW [5], as sketched in Fig. 1a.

The model concept follows the seminal work by J. Tersoff in Ref. [18] (see also [22]). In particular, the intermixing dynamics is restricted within few monolayers from the surface, where activation barriers for atomic exchanges are reasonably low, while the underlying bulk region is assumed immutable and hence it preserves any non-uniform composition profile. As the surface advances during the shell growth, a corresponding amount of material below the mixing region gets buried into the bulk.

Each component of the alloy distributes according to its own incorporation from the gaseous phase, with rate R, and to the local diffusion along the surface, driven by the gradients of chemical potential μ. The net flux of component ν at a given position on the growth front, is then defined as

$$\frac{\partial N_\nu}{\partial t} = R_\nu + \nabla_S \cdot (c_\nu M_\nu \nabla_S \mu_\nu) \qquad (1)$$

where N_ν is the net number of atoms of the ν species moving in time t, M_ν is the mobility of adatoms of species

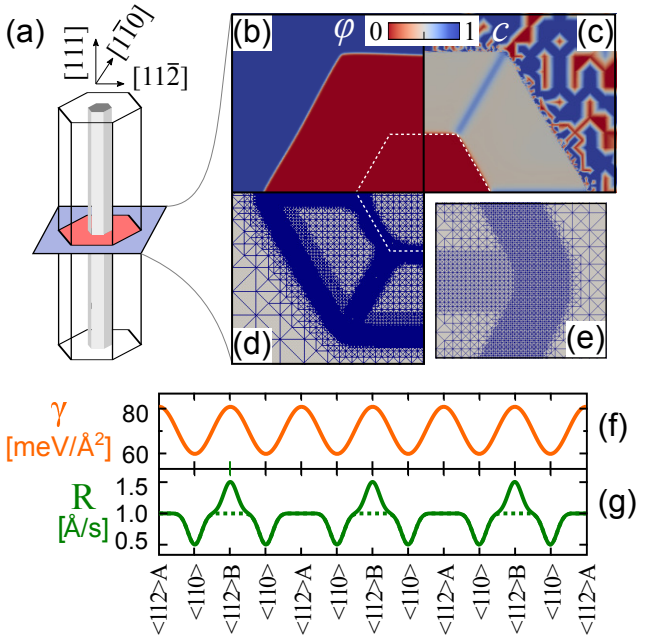

Figure 1: Model definitions. (a) Schematic representation of the 2D (111)-cross-section of the NW as considered in the simulations. A view of (b) the phase-field function φ used for defining the NW shape and of (c) the composition field c tracing the local Al content is shown for a portion of the simulation cell. Notice that c has physical meaning only within the φ=1 solid phase while it changes randomly in the φ=0 vacuum region. (d) Portion of the adaptively refined mesh with (e) a magnification of the corner region between two {110} facets. The initial core geometry, used as starting point for the simulations, is indicated by the white dotted line. Plots of the anisotropic surface energy density γ (f) and growth rate R (g) functions used in the simulations. Both the cases of polar (solid) and non-polar (dashed) <112> orientations is considered.

ν, here assumed to be the same on any facet. c_ν is the local atomic fraction of species ν, such that $\sum_\nu c_\nu = 1$. ∇_S is the surface gradient, i.e. the gradient computed along the surface coordinate. In the present case study, ν can be one of the two alloy cations, i.e. Ga or Al, while the anion As is assumed to immediately bond with both during the layer growth.

By definition, the local chemical potential is the functional derivative of the system free-energy F, here comprising surface energy, edge energy and entropy of mixing:

$$\mu_\nu = \kappa(\gamma + \gamma''(\theta)) - \beta\left(\nabla_S^2\kappa + \frac{1}{2}\kappa^3\right) + \frac{kT}{V_a}\ln c_\nu \qquad (2)$$

The first addendum is the Gibbs-Thompson chemical potential accounting for the surface energy contribution, given by the product of the local profile curvature κ and the surface stiffness $\gamma+\gamma''$, with $\gamma(\theta)$ the (anisotropic) surface energy density. The second addendum accounts for the energy cost of forming an edge between two facets [23], with energy parameter β. The third addendum accounts for the mixing entropy, with k the Boltzmann constant, T the temperature and V_a the volume per atom in the crystalline structure (here assumed to be the same for both species).

Further energetic contributions such as elastic energy or mixing enthalpy are here neglected under the assumption of lattice-matched, ideal alloys.

By combining the fluxes of the two components, it is possible to obtain both the velocity of the growth front along the local surface normal $\hat{\mathbf{n}}$, and the variation in composition c, here given as the Al atomic fraction:

$$v_{\hat{\mathbf{n}}} = R + \nabla_S \cdot [cM_{Al}\nabla_S\mu_{Al} + (1-c)M_{Ga}\nabla_S\mu_{Ga}] \quad (3)$$

$$w\frac{\partial c}{\partial t} = R_{Al} + \nabla_S \cdot (cM_{Al}\nabla_S\mu_{Al}) - cv_{\hat{\mathbf{n}}} \quad (4)$$

where $R = R_{Al} + R_{Ga}$ is the total growth rate and w is the thickness of the mixing region.

In order to efficiently solve the coupled evolution equations here derived, the phase-field (PF) approach [24] of Ref. [25] is exploited. The NW geometry is traced implicitly by the PF function φ , valued 1 in the solid region and 0 in the surrounding vacuum and with a diffuse interface, of thickness ϵ, to smoothly connect them. Nominally, the NW surface is localized by the φ=0.5 iso-line. The composition field c is then extended to the whole domain without any physical meaning in the vacuum region. Figure 1b and c show a typical example of the φ and c fields as appearing in the following simulations.

The motion of the growth front is then defined by the temporal variation of the PF itself over the whole integration domain. By parametrizing eqs. 3 and 4 with respect to φ, and rewriting $\mu_\nu = \mu_\varphi + kT/V_a \ln c_\nu$, with $\mu_\varphi = \delta F/\delta\varphi$, we obtain:

$$\frac{\partial\varphi}{\partial t} = R|\nabla\varphi| + \nabla\cdot\left[\bar{M}\nabla\mu_\varphi\right] + \frac{kT}{V_a}\nabla\cdot\left[\left(\tilde{M}_{Al} - \tilde{M}_{Ga}\right)\nabla c\right] \quad (5)$$

$$\frac{\partial(c\varphi)}{\partial t} = R_{Al}|\nabla\varphi| + \nabla\cdot\left(c\tilde{M}_{Al}\nabla\mu_\varphi\right) + \frac{kT}{V_a}\nabla\cdot\left(\tilde{M}_{Al}\nabla c\right) \quad (6)$$

where $\tilde{M}_\nu = M_\nu(36/\epsilon)\varphi^3(1-\varphi)^2$ is the mobility of component ν, restricted to the surface by the functional dependence on φ (see Ref. [25]), and $\bar{M} = c\tilde{M}_{Al} + (1-c)\tilde{M}_{Ga}$. By using eq. 6 we admit the mixing dynamics to occur only within the $\sim\epsilon$-thick PF interface, where the mobility is non-zero.

According to Ref. [26],

$$\begin{aligned} g(\varphi)\mu_\varphi = &-\epsilon\nabla\cdot[\gamma\nabla\varphi] + \frac{1}{\epsilon}\gamma W'(\varphi) + \\ &-\nabla\cdot\left[\left(\frac{\epsilon}{2}|\nabla\varphi|^2 + \frac{1}{\epsilon}W(\varphi)\right)\nabla_{\nabla\varphi}\gamma\right] + \\ &+\beta\left[-\nabla^2\omega + \frac{1}{\epsilon^2}W''(\varphi)\omega\right] \end{aligned} \quad (7)$$

with the double-well potential $W(\varphi) = 18\varphi^2(1-\varphi)^2$, enforcing the separation of the two phases, solid and vacuum, and $\omega = -\epsilon\nabla^2\varphi + (1/\epsilon)W'(\varphi)$. $g(\varphi) = 30\varphi^2(1-\varphi)^2$ is a stabilizing function [27, 28]. The operator $\nabla_{\nabla\varphi}$ returns the gradient that takes effect along the $\nabla\varphi$ direction. The first three terms in the right-hand side provide the PF equivalent of the Gibbs-Thompson chemical potential in eq. 2 and the last term accounts for the edge contribution, here defined as a Willmore energy [24].

The evolution described by the eqs. 5, 6 and 7 forms a 6^{th} order partial differential equations problem that can be solved numerically by using the finite element method. Here, we use the AMDiS toolbox [29, 30]. Adaptive meshing is exploited to obtain a locally refined mesh, with finer resolution only at the PF interface and in correspondence of regions of compositional changes within the solid phase, as illustrated in the Fig. 1d,e. A maximum mesh resolution of ≈0.07 nm is used so that the PF interface width ϵ can be made as small as 1 nm, which is to be considered the physical limit of the simulations. A semi-implicit time-integration scheme is implemented.

Both the growth rate R and the surface energy density γ are assumed as anisotropic functions depending on the local profile orientation $\hat{\mathbf{n}} = -\nabla\varphi/|\nabla\varphi|$ but independent of the composition c and identical for both species. In the following we will use the realistic 3D notation for facets and directions, even if the actual model is restricted to the 2D (111) cross-section. The convenient formula of Ref. [26] is exploited, allowing to distinguish A and B polar orientations by means of the Heaviside function Θ (see below).

In particular, γ is assumed to only have six minima, corresponding to the six {110} planes of the NW sidewalls:

$$\gamma(\hat{\mathbf{n}}) = \gamma_0\left[1 - \sum_{\hat{\mathbf{m}}_i}^{<110>} a_i(\hat{\mathbf{n}}\cdot\hat{\mathbf{m}}_i)^{1/w_\gamma}\Theta(\hat{\mathbf{n}}\cdot\hat{\mathbf{m}}_i)\right] \quad (8)$$

with $\hat{\mathbf{m}}_i$ the six unit vectors in the <110> directions across the NW sidewalls. We set γ_0=100 meV/Å^2 and a_{110}=0.4 so to have a value of $\gamma(110)$ ≈60 meV/Å^2, compatible with literature data [31], and use w_γ=0.1 to exclude overlap between the minima. A plot of the $\gamma(\hat{\mathbf{n}})$ function is reported in Fig. 1f. The chosen parameters result in a strong anisotropy condition that can be treated numerically only if corner energy is included. A value of corner energy β=10 eV is selected to return a stable evolution with rounding radius of few nms.

The growth rate R is also assumed to have minima in the same {110} planes while maxima are considered for the intermediate <112> orientations:

$$R(\hat{\mathbf{n}}) = R_0\left[1 + \sum_{\hat{\mathbf{m}}_i}^{<110>,<112>} b_i(\hat{\mathbf{n}}\cdot\hat{\mathbf{m}}_i)^{1/w_R}\Theta(\hat{\mathbf{n}}\cdot\hat{\mathbf{m}}_\mathbf{i})\right] \quad (9)$$

with R_0=1 Å/s. The $\hat{\mathbf{m}}_i$ unit vectors includes both the six <110> and the six <112> directions. For the firsts, we set a value of b_{110}=-0.5, so that the growth rate of the {110} facets is 0.5 Å/s, compatibly with experiments. For the seconds, we consider b_{112A}=0 and b_{112B}=+0.5 to deal with the system polarity or simply b_{112}=0 if not needed. A value of $w_R = 0.01$ is set to avoid any overlap between them. A plot of the $R(\hat{\mathbf{n}})$ function is reported in Fig. 1g.

In the present simulations, an AlGaAs shell with nominal composition of 33% Al is grown on a 40 nm wide GaAs core, shaped as a {110} hexagon. A typical growth temperature of 500 °C is considered. To reduce the computational cost, only one half of the NW is considered by imposing a Neumann mirror boundary along its <112> symmetry axis. According to the experimental evidences indicating very slow mobility for Al, we set $M_{Ga} = 100 M_{Al}$. The evolution is entirely controlled by the ratio between growth rate and mobility, here arbitrarily tuned to $2{\cdot}10^{-3}$ to match the experimental behavior.

3. Results and Discussion

In order to identify and understand the key factors responsible for the segregation pattern observed in the experiments it is very instructive to start by building the model with the very minimum number of contributions and parameters. This will allow us to get a qualitative indication of the role played by each term independently, before combining them in a more realistic but complex model.

The {110} faceting of the sidewalls of [111]-oriented III-V core-shell NWs can be well understood on the basis of energetic arguments. First-principle studies in the literature [31] show indeed that {110} are stable facets at variance with the other crystallographic planes running parallel to the NW axis, i.e. the {112} planes, which have higher surface energy and are indeed predicted to break into {110} or other low-index facets [32, 33]. The expected equilibrium Wulff shape in the (111) cross-section is then an {110}-bounded hexagon, compatibly with the experimental observation.

A first, minimal model to inspect the evolution of the shell morphology and the associated effects of compositional segregation can then be devised by considering a uniform deposition rate $R = R_0$ and the anisotropic surface energy $\gamma(\theta)$ defined in eq. 8 to enforce the {110} faceting. This situation is illustrated by the polar-plot in Fig. 2a. The result of such a test simulation is reported in Fig. 2b. Evidently, the shell profile evolves with a {110} faceting, with locally rounded corners. The segregation pattern indicated by the color map is characterized by the formation of narrow stripes radially departing from the core vertices to the outer corners of the shell. Such stripes are however enriched in Ga, returning the exact opposite of the experimental behavior. The explanation is made clear by the analysis of the chemical potential along the surface profile, reported in Fig. 2c. μ is minimum in the <112> direction, i.e. at the corners between the NW facets where the surface energy is maximum, causing a net flow of material from the {110} sides to the corners so to preserve a straight faceting. Since Ga diffuses faster than Al, a slightly higher amount of Ga is then pushed to the corners and buried in the bulk underneath as the front advances. Since the segregation process is locally determined by the balance of surface and edge energy contributions to μ at

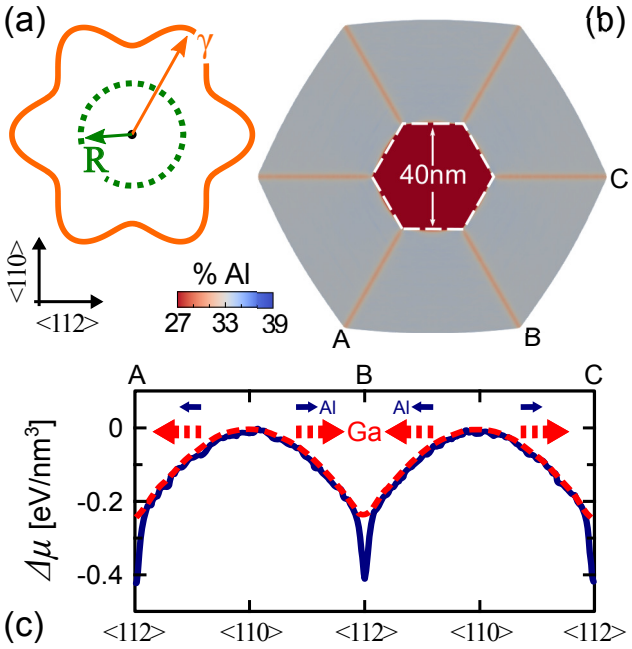

Figure 2: Evolution of an AlGaAs shell under the assumption of anisotropic γ and uniform growth rate R, as reported in polar-plot in panel (a). (b) Simulation profile showing the composition within the shell by color map. The initial GaAs core geometry is shown by dashes. (c) Plot of the surface chemical potential of both Ga and Al referred to the value in the <110> direction. Arrows indicate the direction and magnitude of the diffusion currents.

the corners, it is not modified by the increasing shell thickness, evolving in a steady mode during the whole growth. The width of the segregation stripes is then essentially determined by the rounding radius at the corners, that can be made nm-thin by suitably tuning the β parameter.

While the simulation demonstrates that a {110}-faceted shape can be enforced during growth by material redistribution due to the γ-anisotropy, the resulting segregation is exactly reversed with respect to the experimental one. It is therefore evident that this thermodynamic description is not sufficient to capture the dynamical behavior of the real system.

The very opposite case to be considered for a minimal model of the shell growth is that of kinetic-driven faceting, determined by orientation-dependent growth rate $R(\theta)$. Based on the simple geometric arguments of the kinetic Wulff construction [34, 35, 36], the apparent shape of a growing crystal is determined by those facets with the slowest growth rate. Then, we admit that the growth rate R is minimum in the <110> directions and maximum for all other intermediate orientations. This is a quite reasonable hypothesis also from a physical point of view, consistent with literature studies [3, 37], in particular with the detailed experimental analysis on AlGaAs core-shell NWs in Ref. [6]. There, it is indeed clearly shown that the growth of AlAs shells proceeds at a quite different rate in the <110> and <112> directions, returning a thicker profile around this latter orientations, protruding outward

with respect to the ideal {110}-hexagonal shape.

Then, a test simulation is set by considering the anisotropic growth rate R given in eq. 9, with the simplifying assumption of $b_{112} = 0$ for all <112> directions, and isotropic surface energy $\gamma = \gamma_0$, without any edge contribution, i.e. β=0. These are shown by the polar plot in Fig. 3a. The resulting growth profile, shown in panel (b), is shaped as the desired {110}-hexagon but for a large rounding at the corners. The compositional profile, rendered by the color map, now displays the right direction of segregation: Al rich stripes are indeed formed along the <112> directions, compatibly with experiments, even if substantially wider.

This is promptly understood by looking to the variation of the chemical potential while moving along the growth front, from <112> to <110> directions, plotted in Fig. 3c. Now, there is an excess of material supply at the corners with respect to the {110} facets and this alone would result into outward profile protrusions. This is however very unfavorable from the energetic point of view as corresponding to very high local curvatures, i.e. much higher μ with respect to the {110} planes. A substantial transfer of material away from the corners is then triggered to counter-balance the bias in material supply, resulting in the local smearing of the profile. A stationary condition is then reached, maintaining a constant μ gradient to drive a continuous spill of material out of the corners. Then, due to the its lower mobility, Al will remain behind at the corners while Ga flows away and spreads all along the {110} facets, resulting in the sunburst segregation. As barely distinguishable by the color map, in the first growth stages, when the size of the {110} facets is short enough, the additional amount of Ga spilled-out of the corners causes a slight enhancement of the Ga content in the shell sides with respect to the nominal composition. This effect fades as the length of the facets grows large offering a greater volume for diluting the Ga flux from the corners. At a closer inspection, a local increase in the Ga content is distinguishable right at the sides of the Al-rich stripes, where the diffusion current is maximum.

The previous analysis showed that the only hypothesis of a slower growth kinetics on the {110} facets with respect to the (faster) <112> corner regions provides the leading factor to reproduce the segregation behavior. However, it is reasonable to expect that in the real system both anisotropies in R and γ act simultaneously to return the experimental behavior in a synergistic way: the former determines the direction of the material flux from the corners to the facets, the latter enforces a neatly faceted geometry with a limited corner rounding on the scale of few nanometers.

In order to develop a more realistic description of the actual system, a further analysis of the literature results is to be done. Several studies [3, 12] showed that the actual symmetry of the sunburst segregation is just 3-fold. Polarity effects break the equivalence in the <112> directions returning a different behavior between <112>A and <112>B orientations. A direct evidence is provided

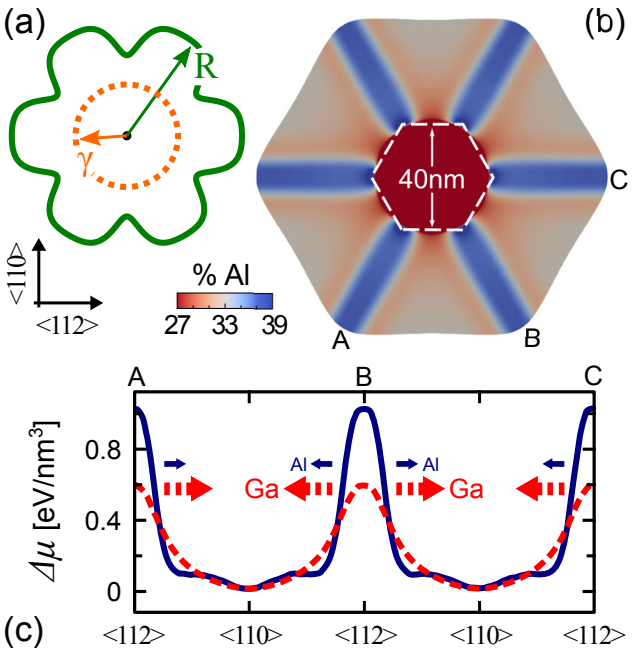

Figure 3: Evolution of an AlGaAs shell under the assumption of orientation dependent growth rate R and isotropic surface energy γ, as reported in the polar-plot in panel (a). (b) Simulation profile showing the composition within the shell by color map. The initial GaAs core geometry is shown by dashes. (c) Plot of the surface chemical potential of both Ga and Al referred to the value in the <110> direction. Arrows indicate the direction and magnitude of the diffusion currents.

by the already cited experiments of AlAs shell growth in Ref. [6], exhibiting more pronounced protrusions in the three <112>B corners rather than in the three <112>A ones. These testifies an enhanced growth rate in the <112>B directions that can be modeled by raising the corresponding maxima in the anisotropic function of R in eq. 9. By using this function in combination with the anisotropic γ of eq. 8, as illustrated by the polar plot in Fig. 4a, it is possible to reproduce the alternating growth of AlAs and GaAs shells as in the experiments of Ref. [6]. An example is reported in the Fig. 4b, showing the simulation result for a multilayered structure grown on the GaAs NW core. Similarly to the experiments, the AlAs layers develop outward pointing protrusions. As made evident in the magnified view in panel c, the corner overgrowth builds up since the first deposition stages, with a major development in the fastest growing <112>B directions (see the profile distortion with respect to the ideal hexagonal front reported by a dashed line). On the contrary, the GaAs shells tend to restore a nearly regular hexagonal shape, even when deposited on the peaked AlAs shape. Such a different behavior between AlAs and GaAs in the simulations is fully determined by their large difference in surface mobility. The former can indeed move only for very short distances so that material is stuck in the directions of major supply, i.e. the <112>, despite energetically unfavorable. The same nonuniform growth rates are assumed also for GaAs

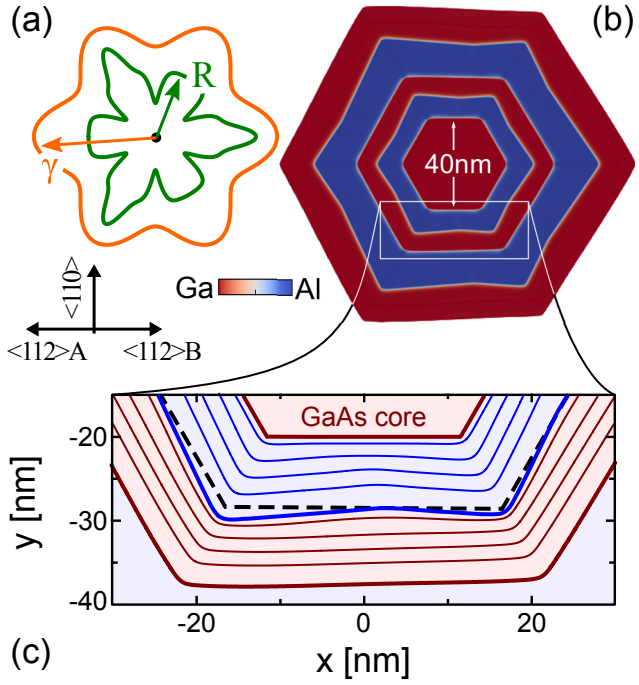

Figure 4: Evolution of a multilayered AlAs-GaAs shell on a GaAs core, under the assumption of both anisotropic γ and R, reported in the polar plot in panel (a). (b) Simulation profile showing the composition within the shell by color map. (c) Magnification of a profile portion including both <112>A and <112>B. The evolution sequence for the first AlAs-GaAs layers is shown by solid lines. The dashed line show an ideal hexagonal shape, to be compared with the outer profile of the first AlAs layer.

but, due to the much longer diffusion length of Ga, surface diffusion spreads all the incoming material over the whole facet length under the push of surface energy anisotropy. Arguably, GaAs may also have an intrinsically lower preference to grow in the <112> directions compared to AlAs but, since the different mobility looks enough to explain the change in morphology, we here neglect such an option.

Once proved the capability of the model in reproducing the experimental evolution of the multilayered structure, it can finally be applied to the growth of the alloyed AlGaAs shell, so to get a more realistic description of the sunburst segregation. The result of such a simulation is shown in the Fig. 5a and closely resembles the experimental evidences [1]. In particular, an almost perfectly hexagonal shell is obtained despite the anisotropic growth rates thanks to the long range material redistribution enabled by the large availability of Ga in the shell. Corners in between the {110} facets are now quite sharp, with rounding radius of ∼3 nm. Al-rich stripes develop right along the <112> directions, from the core to the outer shell corners. For a more quantitative analysis, in panel b we plot the composition variation when moving within the shell along the path AB marked in panel a, passing through both a <112>A and a <112>B corner. There, we see a significant enhancement in the Al content, with a maximum of ≈57% in the <112>B direction, while ≈51% is obtained in the <112>A one, reflecting the difference in growth rate discussed above. The width of the segregation peaks is of the same order of the rounding of the corners, i.e. ∼3-4 nm. It is almost the same for both directions, at variance with experiments reporting thinner stripes in the <112>A direction [3], possibly related to finer details in the anisotropic function and/or slight differences in edge energy, beyond our simple model. All points within the {110} region have the nominal Al content of 33%, with local variations within a ±1%. The radial variation of Al content along the stripes and in the middle of the {110} facets is made evident in the plot of Fig. 5c, where the composition is traced along the <112> and the <110> axis across the NW center. The formation of the Al-rich stripes in the <112>A and <112>B directions is almost immediate and their composition is constant throughout the whole shell thickness. A small deviation below the nominal Al content set by the deposition is instead noticeable in the {110} fronts close to the core region. This is due to the slight dilution of the deposited material with the small amount of Ga spilling out of the corners, producing a visible effect only when the facets are short enough. As the shell thickness increases, the Al content in the middle of the {110} facets converges to the nominal value.

Simulation parameters set for the case in Fig. 5 have been tuned in such a way to achieve a convincing correspondence with the typical experimental observations, still trying to avoid a strict fitting of one specific case to keep the description general. The magnitude and definition of the observed segregation effects are of course dependent on such a parameter choice. Clearly, the key factor to control the Al-content in the stripes comes from the difference in the growth rates between <110> and <112> orientations. The surface energy anisotropy and edge energy also play a key role in controlling the width of the corners. An accurate determination of these material parameters is quite complex, especially for the largely unknown kinetic rates, which may be different for each species and eventually depend on the alloy composition.

The external growth conditions of the experimental environment are also very important. In particular, since the kinetic segregation effects here discussed takes place through surface diffusion, it is a strict requirement to have enough mobility to let the material move before getting permanently incorporated. If diffusion is much limited, as in the case of the AlAs shell considered in Fig. 4, the material will just accumulate on the fast growing fronts with composition determined only by the material supply. On the contrary, if diffusion becomes very fast, e.g. at very high temperature or by post-growth annealing, the entropic tendency toward mixing will blur any segregation profile in the surface region and eventually lead to a more uniform composition.

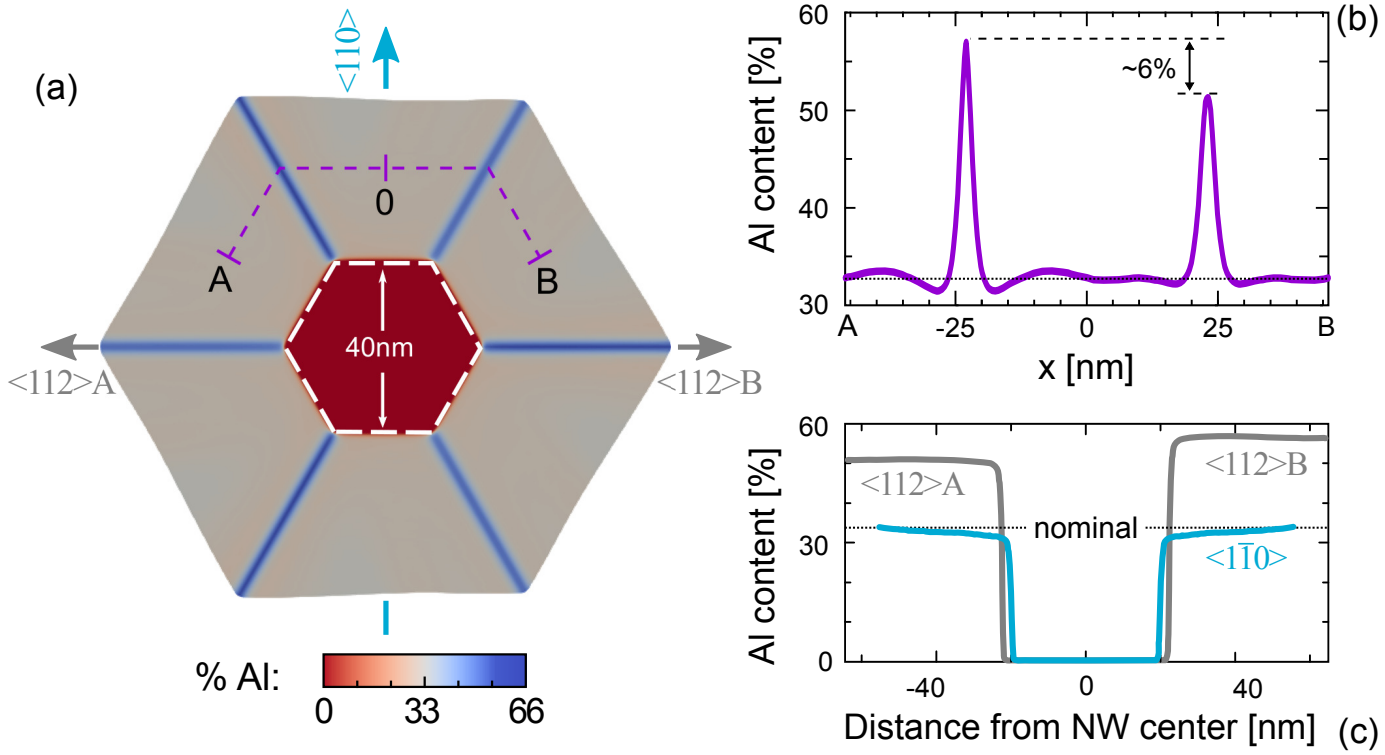

Figure 5: Simulation of sunburst segregation during the growth of the AlGaAs shell, including polarity effects. (a) Simulation profile showing the composition within the shell by color map. The initial core is traced by dashes. (b) Plot of the composition along the AB path dashed in panel a. (c) Plot of the radial variation of composition along the two <112> and the <110> main axis through the NW center. The nominal 33% Al content of deposition is also indicated by a dotted line for reference.

4. Conclusions

In this study the dynamics of sunburst segregation in core-shell NWs has been modeled and simulated by combining the effects of orientation dependent growth rates and surface energy anisotropy, along with the different mobility of the alloy components. It is recognized that an enhancement in the growth rate at the facet edges along the <112> directions is key to induce a material flow away from the corners, leaving behind an excess of the slow diffusing species. The surface energy anisotropy, enforcing the {110} faceting also plays a role in limiting the width of the segregation region to few nms, as in experiments. The distinction between <112>A and <112>B orientations by imposing a faster growth in these latter ones, produces a differentiation in the segregation returning a 3-fold symmetry, consistently with the experiments.

Even if the whole study has been conducted with respect to a GaAs-AlGaAs core-shell NW, setting parameters consistent with it, the overall description is to be considered general and directly extensible to all other III-V systems mentioned in the Introduction, by just tuning the appropriate parameters. Further effects are expected whether the core or the shell are multi-faceted, eventually combining corner segregation effects with the faceting transition [9, 38, 39].

While the analysis here reported is strictly valid for lattice-matched alloys, the sunburst segregation pattern is also recognizable in strained systems. In the case of low-strain systems it is reasonable to expect that the here discussed mechanisms are still the leading ones. For high strain levels the actual contribution of elastic energy to the chemical potential has to be explicitly taken into account. In such a case, a redistribution of the alloy components at the surface may be activated to achieve a better strain relaxation (see e.g. [39, 40]), as corners are expected to better accomodate the misfit with respect to the facets. While the modeling of strain effects is out of the scope of the present study, it is a natural extension of this approach for an upcoming work.

Acknowledgments

We gratefully acknowledge P.W. Voorhees for his comments on the model and interpretation, E.P.A.M. Bakkers for helpful discussions on related phenomena in group-IV nanowires and M. Albani for technical support.

References

[1] M. Heiss, Y. Fontana, A. Gustafsson, G. Wüst, C. Magen, D. D. O'Regan, J. W. Luo, B. Ketterer, S. Conesa-Boj, a. V. Kuhlmann, J. Houel, E. Russo-Averchi, J. R. Morante, M. Cantoni, N. Marzari, J. Arbiol, A. Zunger, R. J. Warburton,

A. Fontcuberta i Morral, Self-assembled quantum dots in a nanowire system for quantum photonics, Nat. Mater. 12 (2013) 439–444. doi:10.1038/nmat3557.

[2] D. Rudolph, S. Funk, M. Döblinger, S. Morkötter, S. Hertenberger, L. Schweickert, J. Becker, S. Matich, M. Bichler, D. Spirkoska, I. Zardo, J. J. Finley, G. Abstreiter, G. Koblmüller, Spontaneous Alloy Composition Ordering in GaAs-AlGaAs CoreShell Nanowires, Nano Lett. 13 (2013) 1522–1527. doi:10.1021/nl3046816.

[3] C. Zheng, J. Wong-Leung, Q. Gao, H. H. Tan, C. Jagadish, J. Etheridge, Polarity-driven 3-fold symmetry of GaAs/AlGaAs core multishell nanowires, Nano Lett. 13 (2013) 3742–3748. doi:10.1021/nl401680k.

[4] N. Jiang, Q. Gao, P. Parkinson, J. Wong-Leung, S. Mokkapati, S. Breuer, H. H. Tan, C. L. Zheng, J. Etheridge, C. Jagadish, Enhanced minority carrier lifetimes in GaAs/AlGaAs core-shell nanowires through shell growth optimization, Nano Lett. 13 (2013) 5135–5140. doi:10.1021/nl4023385.

[5] L. Mancini, Y. Fontana, S. Conesa-Boj, I. Blum, F. Vurpillot, L. Francaviglia, E. Russo-Averchi, M. Heiss, J. Arbiol, A. F. i. Morral, L. Rigutti, Three-dimensional nanoscale study of Al segregation and quantum dot formation in GaAs/AlGaAs core-shell nanowires, Appl. Phys. Lett. 105 (2014) 243106. doi:10.1063/1.4904952.

[6] N. Jeon, D. Ruhstorfer, M. Döblinger, S. Matich, B. Loitsch, G. Koblmüller, L. Lauhon, Connecting Composition-Driven Faceting with Facet-Driven Composition Modulation in GaAs-AlGaAs Core-Shell Nanowires, Nano Lett. 18 (2018) 5179–5185. doi:10.1021/acs.nanolett.8b02104.

[7] J. Treu, T. Stettner, M. Watzinger, S. Morkötter, M. Döblinger, S. Matich, K. Saller, M. Bichler, G. Abstreiter, J. J. Finley, J. Stangl, G. Koblmüller, Lattice-Matched InGaAsInAlAs CoreShell Nanowires with Improved Luminescence and Photoresponse Properties, Nano Lett. 15 (2015) 3533–3540. doi:10.1021/acs.nanolett.5b00979.

[8] K. Tomioka, M. Yoshimura, T. Fukui, A IIIV nanowire channel on silicon for high-performance vertical transistors, Nature 488 (2012) 189–192. doi:10.1038/nature11293.

[9] N. Sköld, J. B. Wagner, G. Karlsson, T. Hernán, W. Seifert, M.-E. Pistol, L. Samuelson, Phase Segregation in AlInP Shells on GaAs Nanowires, Nano Lett. 6 (2006) 2743–2747. doi:10.1021/nl061692d.

[10] J. B. Wagner, N. Sköld, L. Reine Wallenberg, L. Samuelson, Growth and segregation of GaAsAlxIn1xP core-shell nanowires, J. Cryst. Growth 312 (2010) 1755–1760. doi:10.1016/j.jcrysgro.2010.02.009.

[11] L. Balaghi, G. Bussone, R. Grifone, R. Hübner, J. Grenzer, M. Ghorbani-Asl, A. V. Krasheninnikov, H. Schneider, M. Helm, E. Dimakis, Widely tunable GaAs bandgap via strain engineering in core/shell nanowires with large lattice mismatch, Nat. Commun. 10 (2019) 2793. doi:10.1038/s41467-019-10654-7.

[12] Y. Zhang, A. M. Sanchez, J. Wu, M. Aagesen, J. V. Holm, R. Beanland, T. Ward, H. Liu, Polarity-driven quasi-3-fold composition symmetry of self-catalyzed III-V-V ternary core-shell nanowires, Nano Lett. 15 (2015) 3128–3133. doi:10.1021/acs.nanolett.5b00188.

[13] S. Assali, A. Dijkstra, A. Li, S. Koelling, M. A. Verheijen, L. Gagliano, N. Von Den Driesch, D. Buca, P. M. Koenraad, J. E. Haverkort, E. P. Bakkers, Growth and Optical Properties of Direct Band Gap Ge/Ge0.87Sn0.13 Core/Shell Nanowire Arrays, Nano Lett. 17 (2017) 1538–1544. doi:10.1021/acs.nanolett.6b04627.

[14] M. Albani, S. Assali, M. A. Verheijen, S. Koelling, R. Bergamaschini, F. Pezzoli, E. P. A. M. Bakkers, L. Miglio, Critical strain for Sn incorporation into spontaneously graded Ge/GeSn core/shell nanowires, Nanoscale 10 (2018) 7250–7256. doi:10.1039/C7NR09568F.

[15] L. Steinke, P. Cantwell, D. Zakharov, E. Stach, N. J. Zaluzec, A. Fontcuberta i Morral, M. Bichler, G. Abstreiter, M. Grayson, Nanometer-scale sharpness in corner-overgrown heterostructures, Appl. Phys. Lett. 93. doi:10.1063/1.2988526.

[16] G. Tutuncuoglu, M. De la Mata, D. Deiana, H. Potts, F. Matteini, J. Arbiol, A. Fontcuberta i Morral, Towards defect-free 1-D GaAs/AlGaAs heterostructures based on GaAs nanomembranes, Nanoscale 7 (2015) 19453–19460. doi:10.1039/C5NR04821D.

[17] G. Biasiol, E. Kapon, Mechanisms of Self-Ordering of Quantum Nanostructures Grown on Nonplanar Surfaces, Phys. Rev. Lett. 81 (1998) 2962–2965. doi:10.1103/PhysRevLett.81.2962.

[18] J. Tersoff, Kinetic surface segregation and the evolution of nanostructures, Appl. Phys. Lett. 83 (2003) 353–355. doi:10.1063/1.1592304.

[19] Q. Zhang, J.-N. Aqua, P. W. Voorhees, S. H. Davis, Mechanisms of morphological evolution on faceted coreshell nanowire surfaces, J. Mech. Phys. Solids 91 (2016) 73–93. doi:10.1016/j.jmps.2016.02.033.

[20] Q. Zhang, P. W. Voorhees, S. H. Davis, Mechanisms of surface alloy segregation on faceted core-shell nanowire growth, J. Mech. Phys. Solids 100 (2017) 21–44. doi:10.1016/j.jmps.2016.12.005.

[21] D. Alpay, L. Peng, L. D. Marks, Are Nanoparticle Corners Round?, J. Phys. Chem. C 119 (2015) 21018–21023. doi:10.1021/acs.jpcc.5b07021.

[22] R. Bergamaschini, J. Tersoff, Y. Tu, J. J. Zhang, G. Bauer, F. Montalenti, Anomalous Smoothing Preceding Island Formation During Growth on Patterned Substrates, Physical Review Letters 109 (2012) 156101. doi:10.1103/PhysRevLett.109.156101.

[23] B. J. Spencer, Asymptotic solutions for the equilibrium crystal shape with small corner energy regularization, Phys. Rev. E 69 (2004) 011603. doi:10.1103/PhysRevE.69.011603.

[24] B. Li, J. Lowengrub, A. Voigt, Geometric Evolution Laws for Thin Crystalline Films: Modeling and Numerics, Commun. Comput. Phys. 6 (2009) 433–482.

[25] R. Backofen, R. Bergamaschini, A. Voigt, The interplay of morphological and compositional evolution in crystal growth: a phase-field model, Philos. Mag. 94 (19) (2014) 2162. doi:10.1080/14786435.2014.907510.

[26] M. Salvalaglio, R. Backofen, R. Bergamaschini, F. Montalenti, A. Voigt, Faceting of Equilibrium and Metastable Nanostructures: A Phase-Field Model of Surface Diffusion Tackling Realistic Shapes, Cryst. Growth Des. 15 (2015) 2787–2794. doi:10.1021/acs.cgd.5b00165.

[27] C. Gugenberger, R. Spatschek, K. Kassner, Comparison of phase-field models for surface diffusion, Phys. Rev. E 78 (2008) 016703. doi:10.1103/PhysRevE.78.016703.

[28] R. Backofen, S. M. Wise, M. Salvalaglio, A. Voigt, Convexity splitting in a phase field model for surface diffusion, Int. J. Numer. Anal. Mod. 16 (2019) 192–209.

[29] S. Vey, A. Voigt, AMDiS: adaptive multidimensional simulations, Comput. Vis. Sci. 10 (2007) 57–67. doi:10.1007/s00791-006-0048-3.

[30] T. Witkowski, S. Ling, S. Praetorius, A. Voigt, Software concepts and numerical algorithms for a scalable adaptive parallel finite element method, Adv. Comput. Math. 41 (2015) 1145–1177. doi:10.1007/s10444-015-9405-4.

[31] N. Moll, A. Kley, E. Pehlke, M. Scheffler, GaAs equilibrium crystal shape from first principles, Phys. Rev. B 54 (1996) 8844–8855. doi:10.1103/PhysRevB.54.8844.

[32] D. J. Chadi, Atomic and electronic structures of (111), (211), and (311) surfaces of GaAs, J. Vac. Sci. Technol. B 3 (1985) 1167. doi:10.1116/1.583033.

[33] K. Jacobi, J. Platen, C. Setzer, J. Maárquez, L. Geelhaar, C. Meyne, W. Richter, A. Kley, P. Ruggerone, M. Scheffler, Morphology, surface core-level shifts and surface energy of the faceted GaAs(112)A and (112)B surfaces, Surf. Sci. 439 (1999) 59–72. doi:10.1016/S0039-6028(99)00713-X.

[34] S. H. Jones, L. S. Salinas, Generalized simulator for vapor phase epitaxy on patterned substrates, J. Cryst. Growth 154 (1995) 163–171. doi:10.1016/0022-0248(95)00884-5.

[35] J. W. Cahn, W. C. Carter, Crystal Shapes and Phase Equilibria:

A Common Mathematical Basis, Metall. Mater. Trans. A 27A (1996) 1431–1440. doi:10.1007/BF02649804.

[36] M. Albani, R. Bergamaschini, M. Salvalaglio, A. Voigt, L. Miglio, F. Montalenti, Competition Between Kinetics and Thermodynamics During the Growth of Faceted Crystal by Phase Field Modeling, Phys. Status Solidi B 256 (2019) 1800518. doi:10.1002/pssb.201800518.

[37] M. Albani, L. Ghisalberti, R. Bergamaschini, M. Friedl, M. Salvalaglio, A. Voigt, F. Montalenti, G. Tütüncüoglu, A. Fontcuberta i Morral, L. Miglio, Growth kinetics and morphological analysis of homoepitaxial GaAs fins by theory and experiment, Phys. Rev. Materials 2 (2018) 093404. doi:10.1103/PhysRevMaterials.2.093404.

[38] S. Conesa-Boj, D. Kriegner, X.-l. Han, S. Plissard, X. Wallart, J. Stangl, A. Fontcuberta i Morral, P. Caroff, Gold-Free Ternary IIIV Antimonide Nanowire Arrays on Silicon: Twin-Free down to the First Bilayer, Nano Lett. 14 (2014) 326–332. doi:10.1021/nl404085a.

[39] L. Gagliano, A. Belabbes, M. Albani, S. Assali, M. A. Verheijen, L. Miglio, F. Bechstedt, J. E. Haverkort, E. P. Bakkers, Pseudodirect to Direct Compositional Crossover in Wurtzite GaP/InxGa1-xP Core-Shell Nanowires, Nano Lett. 16 (2016) 7930–7936. doi:10.1021/acs.nanolett.6b04242.

[40] L. Francaviglia, G. Tütüncüoglu, S. Martí-Sánchez, E. Di Russo, S. Escobar Steinvall, J. Segura Ruiz, H. Potts, M. Friedl, L. Rigutti, J. Arbiol, A. Fontcuberta i Morral, Segregation scheme of indium in AlGaInAs nanowire shells, Phys. Rev. Materials 3 (2019) 023001. doi:10.1103/PhysRevMaterials.3.023001.